Tellus (2008), 60B, 82–97
Printed in Singapore. All rights reserved

TELLUS

Climatic response to anthropogenic sulphate aerosols versus well-mixed greenhouse gases from 1850 to 2000 AD in CLIMBER-2

By EVA BAUER[1]*, VLADIMIR PETOUKHOV[1], ANDREY GANOPOLSKI[1] and ALEXEY V. ELISEEV[2], [1]*Potsdam Institute for Climate Impact Research, PO Box, 60 12 03, D-14412 Potsdam, Germany;* [2]*A.M. Obukhov Institute of Atmospheric Physics RAS, Moscow, Russia*

(Manuscript received 3 April 2007; in final form 6 August 2007)

ABSTRACT

The Earth system model CLIMBER-2 is extended by a scheme for calculating the climatic response to anthropogenic sulphur dioxide emissions. The scheme calculates the direct radiative forcing, the first indirect cloud albedo effect, and the second indirect cloud lifetime effect induced by geographically resolved sulphate aerosol burden. The simulated anthropogenic sulphate aerosol burden in the year 2000 amounts to 0.47 TgS. The best guesses for the radiative forcing due to the direct effect are -0.4 W m^{-2} and for the decrease in short-wave radiation due to all aerosol effects -0.8 W m^{-2}. The simulated global warming by 1 K from 1850 to 2000 caused by anthropogenic greenhouse gases reduces to 0.6 K when the sulphate aerosol effects are included. The model's hydrological sensitivity of 4%/K is decreased by the second indirect effect to 0.8%/K. The quality of the geographically distributed climatic response to the historic emissions of sulphur dioxide and greenhouse gases makes the extended model relevant to computational efficient investigations of future climate change scenarios.

1. Introduction

In the last century, the atmospheric concentrations of greenhouse gases and aerosols from anthropogenic activity increased considerably, thus causing a growing concern about their impact on the climate system. Noteworthy are the growing concentrations of greenhouse gases such as carbon dioxide (CO_2), methane (CH_4), nitrous oxide (N_2O) and the chlorofluorocarbons CFC-11 and CFC-12 and the changes in the tropospheric distribution of sulphate aerosols. Investigations with different climate models, ranging from simple models with a coarse resolution to sophisticated general circulation models (GCMs), show that the anthropogenically induced climate changes in recent decades clearly distinguish from natural climate changes (see IPCC, 2001, and references therein). Natural climate changes in the last millennium before 1850 AD were largely caused by solar variability and volcanic activity, but after 1850 AD the climate system is increasingly influenced by anthropogenic activity (e.g. Crowley, 2000).

Sulphate aerosols cause a tendency of cooling due to their direct and indirect effects exerted on the solar radiative fluxes (e.g. Charlson et al., 1992; Chuang et al., 1997). Hence, the sulphate aerosol effects can partly compensate the enhanced global warming generated by the long-wave absorption of the anthropogenic greenhouse gases. In some regions, the temperature rise from anthropogenic greenhouse gases may possibly even be overcompensated by the aerosol cooling effect. The imbalance between the temperature changes from the sulphate aerosol forcing and greenhouse gas forcing is a subject of intense studies with the use of three-dimensional (3-D) atmospheric models (Kiehl and Briegleb, 1993; Taylor and Penner, 1994; Kiehl et al., 2000; Quaas et al., 2004) and coupled atmosphere-ocean models (Haywood et al., 1997; Roeckner et al., 1999; Johns et al., 2003; Harvey, 2004). In climate change simulations, the greenhouse gases released from fossil fuel burning and industrial activity are considered to be well mixed in the atmosphere, and global and annual mean gas concentrations can be used. The simulation of climate changes due to anthropogenic sulphur dioxide emissions, however, has to account for the inhomogeneous space–time distribution of sulphate aerosols. The differences in the patterns are related to the different lifetimes, that is, up to centuries for the greenhouse gases and a few days for the sulphate aerosols due to their relatively fast deposition rate.

Results from climate change simulations are often difficult to compare. One reason is that model studies span different time periods and therefore deal with different concentrations of

*Corresponding author.
e-mail: eva.bauer@pik-potsdam.de
DOI: 10.1111/j.1600-0889.2007.00318.x

greenhouse gases and sulphate aerosols. The simulations also differ in the description of the sulphate aerosol distribution. Either the sulphate aerosol burden is prescribed (Kiehl and Briegleb, 1993; Haywood et al., 1997; Quaas et al., 2004) or a sulphur cycle model is used (Taylor and Penner, 1994; Roeckner et al., 1999; Kiehl et al., 2000; Johns et al., 2003). Finally, some studies consider only the direct sulphate aerosol effect, while others explore the direct effect together with the first indirect effect or together with the indirect effects on clouds. Nonetheless, simulation studies provide useful information on expected ranges of the aerosol radiative forcing and induced climate changes. The general finding is that the sulphate aerosols produce a stronger cooling in the Northern Hemisphere (NH) than in the Southern Hemisphere (SH), and a stronger cooling during northern summer than during northern winter (e.g. Feichter et al., 1997; Kiehl et al., 2000; Ming et al., 2005).

Yet, there are still open questions about implications related to the space–time inhomogeneity of the cooling from sulphate aerosols and the warming from greenhouse gases. In particular, the basic reasons for the well-marked seasonality in the indicated effects, and the role different climatic feedbacks play in the spatial inhomogeneity of the response to the forcing by aerosols and greenhouse gases are not fully understood. In this paper, we aim at highlighting some aspects of the problem with the use of CLIMBER-2 (Petoukhov et al., 2000; Ganopolski et al., 2001), which is an Earth system model of intermediate complexity (EMIC). We also demonstrate the robustness of our results by comparison with analogous results from more complex general circulation models.

CLIMBER-2 consists of interactively coupled modules for the atmosphere, the ocean and the vegetation. The atmospheric grid has a resolution of 10° in latitude and about 51° in longitude. The atmospheric circulation is calculated in 10 layers and the radiative long-wave fluxes are computed on 16 levels. The integration time step is 1 d using the daily and latitudinal resolved insolation and solar zenith angle. The ocean consists of the zonal mean basins of the Atlantic, the Indian and the Pacific Oceans which are coupled through the Southern Ocean. The oceanic circulation is calculated with a meridional resolution of 2.5° and in 20 layers with vertically increasing thickness, using a 5-d time step. In the land surface scheme, fractions of the major vegetation types, that is, grass and forest, are determined for each grid cell on a yearly time step. The relatively low resolution and the parameterization of the fast (synoptic) atmospheric dynamics allows for running the model over millennial time periods and for integrated modelling purposes within a practical time frame.

CLIMBER-2 simulations of the modern climate (Petoukhov et al., 2000; Ganopolski et al., 2001), the climate of the last glacial maximum (Ganopolski et al., 1998a), and the climate changes during the Holocene (Ganopolski et al., 1998b; Claussen et al., 1999; Brovkin et al., 2002) agree on large-scales with observations and GCM simulations within error bounds. CLIMBER-2 was also applied for analysing the climate changes of the last millennium (Bauer et al., 2003; Bauer and Claussen, 2006) and of future warming scenarios (Rahmstorf and Ganopolski, 1999). The climate sensitivity of CLIMBER-2 derived from equilibrium experiments with CO_2 concentrations of 280 and 560 ppm is 2.6 K. This value is centred in the range from 1.75 to 3.6 K obtained in the EMIC Intercomparison Project (Petoukhov et al., 2005) and the uncertainty range of the climate sensitivity is 1.2–4.3 K (Schneider von Deimling et al., 2006).

So far, the sulphate aerosol effects from space–time varying anthropogenic sulphur dioxide emissions were not investigated with CLIMBER-2. To overcome this shortcoming, we propose an upgrade of the CLIMBER-2 model to calculate the direct as well as the first and second indirect sulphate aerosol effects of anthropogenic sulphate aerosol burdens. The direct effect due to backscattering of solar radiation is calculated in line with the concept of Charlson et al. (1991). The calculation of the first indirect effect, that is, the cloud albedo effect, and the second indirect effect, that is, the cloud lifetime effect, are based on a relation between the concentrations of cloud droplets and aerosol particles (Jones et al., 1994). The climatic response to the sulphate aerosol effects is studied in a series of transient simulations using the anthropogenic sulphur dioxide emission data over the period 1850–2000 AD by Lefohn et al. (1999) and Smith et al. (2001). The aerosol-driven simulations are complemented by including the growing greenhouse gas concentrations. We apply in CLIMBER-2 the so-called equivalent CO_2 ($^{eq}CO_2$) concentration which is the CO_2 concentration increased by the equivalent CO_2 contributions from the trace gases CH_4, N_2O, CFC-11 and CFC-12 (Myhre et al., 1998). Thus the CO_2 concentration which grows from 284.5 to 368.2 ppm over 1850–2000, leads to an increasing $^{eq}CO_2$ concentration from 287.3 to 431.4 ppm over the 150 yr. In the present study, the anthropogenic effects from aerosols other than sulphate, ozone and land use and the natural effects from solar and volcanic activity are not considered.

The analysis of the CLIMBER-2 simulations focuses on the large-scale regional and seasonal responses of the climate to the sulphate aerosol forcing and the greenhouse gas forcing. The next Section 2 describes the transformation of the anthropogenic sulphur dioxide emission data into the atmospheric mass burden of sulphate aerosols and introduces the physical-based schemes for the calculation of the direct and the indirect sulphate aerosol effects. Section 3 analyses the radiative forcing caused by the anthropogenic sulphate aerosol burden and the induced climatic changes from combining the forcing by sulphate aerosols and greenhouse gases. Conclusions are drawn in the final Section 4.

2. Sulphur data and basic sulphate aerosol effects

2.1. Calculation of sulphate aerosol burden

The global emissions of sulphur dioxide (SO_2) from fossil fuel combustion and industrial processes have increased from about

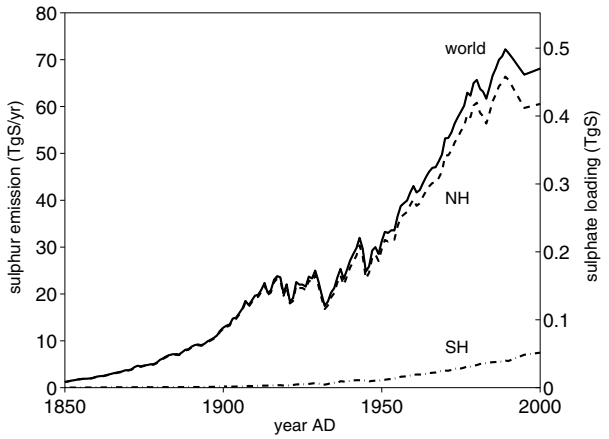

Fig. 1. Time series of anthropogenic sulphur dioxide emissions in TgS yr^{-1} and sulphate aerosol loading in TgS for the world, the NH and the SH over 1850–2000.

1.2 TgS yr^{-1} in 1850 to 68 TgS yr^{-1} in 2000 AD (Tg $= 10^{12}$ g). Over the years, the source strength of the global SO_2 emission and the region of maximum SO_2 emission changed considerably. In 1989, a maximum in the global source strength of 72 TgS yr^{-1} occurred.

Here, we use the annual inventories of the country-based anthropogenic emission data by Lefohn et al. (1999) for the period 1850–1990 and by Smith et al. (2001) for the period 1980–2000. The two time series of emission patterns are spliced to obtain a series of annual emission patterns from 1850 to 2000. Fig. 1 displays the time series of the globally aggregated SO_2 emissions in TgS yr^{-1} together with the partitions for the NH and the SH. The NH emissions are seen to be roughly eight times as large as the SH emissions.

For the subsequent simulations, the country-based anthropogenic SO_2 emissions are distributed among the atmospheric grid cells of CLIMBER-2 under the condition of mass conservation. The SO_2 emissions are transformed to atmospheric mass burdens of sulphate aerosols under the assumption that the coarse resolution of the model grid and the short lifetimes of the aerosols justify the neglect of advective and diffusive processes. Thus the column burden B of sulphate aerosols per grid box area is

$$B = E\,\tau_a\,c_m/A, \tag{1}$$

where E is the mass of sulphur emitted per unit time to a grid box, A is the surface area of the grid box, and τ_a is the effective lifetime of sulphate aerosols. The column burden B is expressed in terms of sulphate aerosol mass [g(SO_4) m^{-2}] by using the mass conversion factor $c_m = 3$, which accounts for the trifold molecular weight of SO_4^{2-} compared to the molecular weight of S. We prescribe an effective lifetime, $\tau_a = 2.5$ d. The value of τ_a incorporates the loss of the precursor gas deposited to the ground and the atmospheric turnover time of sulphate aerosols. Aerosol cycle models yield for sulphate aerosols a mean turnover time of 4.12 d and an estimate of the precursor gas loss of 38% (Textor et al., 2006). These values lead to an effective lifetime of 2.6 d which is close to the corresponding value of 2.7 d given in IPCC (2001). We implicitly assume that the SO_2 oxidation and deposition processes are constant throughout the year.

The global sulphate aerosol loading in TgS (Fig. 1) obtained from the anthropogenic SO_2 emissions (eq. 1) agree with the sulphate burdens computed with a sulphur cycle model over 1850–2000 by Boucher and Pham (2002). The global mean anthropogenic emission of 68 TgS yr^{-1} in the year 2000 corresponds to a global sulphate aerosol loading of 0.47 TgS. This loading compares also well with the anthropogenic part of the sulphate aerosol loading in Stier et al. (2005) which amounts to 60% of the total sulphate loading of 0.8 TgS in 2000. The anthropogenic sulphate aerosol loading of 0.47 TgS corresponds to 1.41 Tg(SO_4) and to a global mean column burden per area of $B_G = 2.8$ mg(SO_4) m^{-2}. Again, the value of $B_G = 2.8$ mg(SO_4) m^{-2} is well in the range of the anthropogenic sulphate burdens given in (table 6.4 IPCC, 2001) which extends from 1.14 to 4 mg m^{-2}, and is in the range obtained by the AeroCom initiative (Schulz et al., 2006).

In practice, the actual column burden from anthropogenic sources in a grid box can exceed the global mean column burden by an order of magnitude. The patterns of the anthropogenic sulphate aerosol burden evolve with the industrial development, as seen by the drift of the maximum sulphate aerosol burden from Europe in 1989 to Southeast Asia in 2000 (Fig. 2). The temporally changing patterns of the sulphate aerosols are of relative importance in the calculation of the sulphate aerosol effects since the induced radiative effects depend not only on the aerosol concentration but also on the ambient climate system properties, such as surface albedo, insolation and cloudiness.

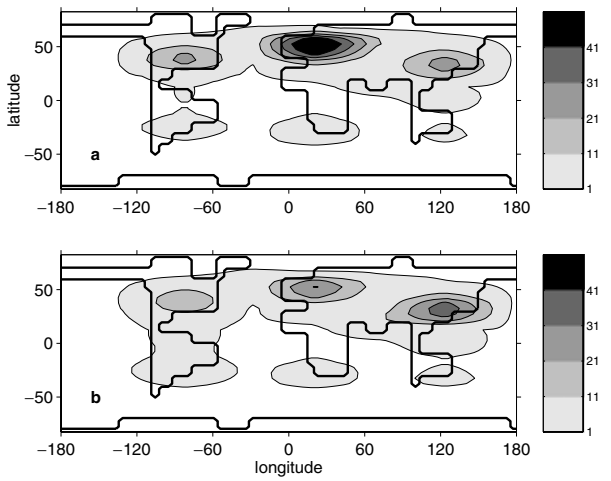

Fig. 2. Geographical distribution of sulphate aerosol mass burden B [mg(SO_4) m^{-2}] aggregated on CLIMBER-2 grid shown for (a) 1989 and (b) 2000.

2.2. Direct sulphate aerosol effect

Anthropogenic sulphate aerosols in the atmosphere induce a negative radiative forcing (direct effect, DE) because sulphate aerosol particles scatter short-wave radiation essentially with no absorption. The upscattering of the insolation by sulphate aerosols is related to an increase in the global and annual mean planetary albedo, $\widetilde{a_p}$, of the Earth–atmosphere system. (We use $\widetilde{\cdot}$ to indicate global and annual averaging.) An increase in the planetary albedo by $\Delta\widetilde{a_p}$ corresponds to a decrease in insolation by $\Delta\widetilde{F} = -(S_0/4)\Delta\widetilde{a_p}$, where S_0 is the solar constant. In the context of radiative forcing, sulphate aerosols from anthropogenic emissions can be treated as an optically thin layer (aerosol optical thickness $\delta_a \ll 1$) located in the near-surface troposphere. In that case, the global and annual mean of the radiative forcing at the top of the atmosphere (TOA) from the direct effect of sulphate aerosols with no absorption is assessed to a first approximation (Charlson et al., 1991, 1992)

$$\Delta\widetilde{F_R} = -\frac{S_0}{2}\,\widetilde{T_i}^2(1-\widetilde{A_c})\,(1-\widetilde{a_s})^2\,\widetilde{\beta}\,\widetilde{\delta_a}, \tag{2}$$

where $\widetilde{T_i}$, $\widetilde{A_c}$, $\widetilde{a_s}$, $\widetilde{\beta}$ and $\widetilde{\delta_a}$ are global and annual mean values of, respectively, transmittance for the solar radiation in the atmosphere above the aerosol layer, cloud fraction, albedo of the Earth's surface, fraction of the insolation scattered upward by sulphate aerosols and their scattering optical thickness. Thus the direct radiative forcing due to a sulphate aerosol layer increases with increasing $\widetilde{\delta_a}$ and $\widetilde{T_i}$, and with decreasing $\widetilde{A_c}$ and $\widetilde{a_s}$. The scattering optical thickness $\widetilde{\delta_a}$ in eq. (2) can be estimated by the product of the mass scattering coefficient $\widetilde{\sigma}$ and the column burden $\widetilde{B}$ of the sulphate mass (Charlson et al., 1991)

$$\widetilde{\delta_a} = \widetilde{\sigma}\,\widetilde{B}. \tag{3}$$

According to eq. (3), the global and annual mean sulphate aerosol optical thickness in 2000 is $\widetilde{\delta_a} = 0.01$ when using for $\widetilde{B}$ the anthropogenic burden $B_G = 2.8$ mg(SO_4) m^{-2} and a mass scattering efficiency $\widetilde{\sigma} = 3.5$ m^2 g^{-1} which is the central value in the uncertainty range for polluted continental aerosols at wavelength 0.55 μm (IPCC, 2001, Table 5.10a). The value of $\widetilde{\delta_a} = 0.01$ lies close to optical depths determined for sulphate aerosols in 2000 relative to 1750 by the AeroCom initiative. The optical depth range for the total sulphate aerosol loading is 0.015–0.051 (Kinne et al., 2006) and the optical depth range for anthropogenic sulphate aerosols is 0.006–0.042 (Schulz et al., 2006).

Typical values for eq. (2) are $\widetilde{T_i} = 0.76$ (Charlson et al., 1992), $\widetilde{\beta} = 0.23$ (IPCC, 2001, table 5.10a), $S_0 = 1365$ W m^{-2} and from a CLIMBER-2 simulation for present climate conditions (see Section 3.2), $\widetilde{a_s} = 0.155$ and $\widetilde{A_c} = 0.65$. Inserting the above values in eq. (2) yields $\Delta\widetilde{F_R} = -0.23$ W m^{-2}. However, $\Delta\widetilde{F_R}$ based on eq. (2) represents a rough approximation as, for instance, the contribution from the cloudy atmosphere is neglected and differing shares from the inhomogeneous spatial distribution of sulphate aerosols and ambient climate conditions are ignored (e.g. Boucher et al., 1998). Actually, the local direct radiative forcing of the sulphate aerosols can differ substantially from the global mean because of space–time variations in solar radiation, solar zenith angle, scattering optical thickness of aerosols, albedo of the Earth's surface and cloudiness. 3-D atmospheric models (see IPCC, 2001, table 6.4) yield for the direct radiative forcing due to anthropogenic sulphate aerosols values between -0.28 and -0.82 W m^{-2} and the AeroCom initiative presents values between -0.19 and -0.96 W m^{-2} (Schulz et al., 2006).

The short-wave scheme of CLIMBER-2 computes the atmospheric transmittance of the solar radiation as a function of water vapour, carbon dioxide, liquid cloud water and background aerosol content using the solar radiation and the solar zenith angle on a daily time step for each grid cell (Petoukhov et al., 2000). We adopt the approach of Charlson et al. (1991) to compute regional and seasonal resolved climate changes from the anthropogenic sulphur emissions. This implies for the computation of the local DE the introduction of the combined surface–aerosol albedo

$$a_{sa} = a_a + T_a^2\,a_s\left[1 + a_a a_s + (a_a a_s)^2 + \cdots\right], \tag{4}$$

where a_s and a_a denote the local values, respectively, of the albedo of the Earth's surface and the albedo of the near-surface sulphate aerosol layer while $T_a = 1 - a_a$ is the transmittance of the sulphate aerosol layer on the assumption that the short-wave radiation is not absorbed by sulphate aerosols. The combined albedo a_{sa} in eq. (4) describes multiple reflections between the aerosol layer and the surface which is expressed by

$$a_{sa} = a_a + \frac{T_a^2\,a_s}{1 - a_a a_s}. \tag{5}$$

The combined albedo a_{sa} substitutes for the surface albedo a_s of each grid cell in the short-wave radiation scheme of the upgraded CLIMBER-2 model. Eq. (5) reveals that a_{sa} increases with a_a, and that a_{sa} reduces to the surface albedo a_s when the aerosol burden vanishes. For a given a_a the lower a_s is, the larger is the difference $a_{sa} - a_s$. This implies a larger cooling for sulphate aerosols above dark surfaces than for sulphate aerosols above bright surfaces. Following Charlson et al. (1991), the aerosol albedo is

$$a_a = \beta\,\delta_a\,\sec\theta, \tag{6}$$

where δ_a is given by eq. (3), but with local sulphate aerosol burden B and local mass scattering coefficient σ in the right side of eq. (3), β is the local upscatter fraction of the insolation, and $\sec\theta$ is the secant of the local solar zenith angle θ. Eq. (6) applies for the direct solar radiation in clear sky conditions, and in cloudy conditions θ is replaced by the effective zenith angle θ_e with characteristic value $\sec\theta_e = 1.66$ (Liou, 1992).

The local sulphate aerosol mass scattering efficiency σ and upscatter fraction β depend on the microphysical properties of particle size distribution, aerosol composition, and relative

Table 1. Parameters for calculation of sulphate aerosol effects and effective parameter values used in the presented simulations

Parameter	Effective value
Lifetime of aerosols	$\tau_a = 2.5$ d
Aerosol scale height	$H_a = 1500$ m
Upscatter fraction	$\beta = 0.23$
Scattering efficiency	$\sigma = 3.5$ m^2 g^{-1}
Natural CCN number conc.	$N_a^{\text{nat}} = 75 \times 10^6$ m^{-3}
Aerosol radius[a]	$r_a = 0.15\,\mu$m

[a]Simulation results of indirect sulphate aerosol effects are also presented for $r_a = 0.1\,\mu$m.

humidity (RH) (Chylek and Wong, 1995; Nemesure et al., 1995; Pilinis et al., 1995; Boucher et al., 1998). The dependence of β on the solar zenith angle and the aerosol phase function of light scattering is implicitly included by an average over the solar zenith angle. Sulphate aerosol particles which reside in the size range of the accumulation mode (particle radii between 0.05 and 1 μm) are hygroscopic and their size grows with increasing RH (Li et al., 2001; Takemura et al., 2005; Randriamiarisoa et al., 2006). For solar wavelengths, an increase in the particle radius is accompanied, on the one hand, with an increase in σ, and on the other hand, with a decrease in β. The range of uncertainty in the radiative forcing due to changes in σ and β with changes in RH and particle size can be estimated based on the uncertainty ranges for σ from 2.3 to 4.7 m^2 g^{-1} and for β from 0.17 to 0.29 (IPCC, 2001, table 5.10a). Hence, from eqs (2) and (3) a lower value of the direct radiative forcing $\Delta\widetilde{F_R}$, representative for dry aerosol particles, can be estimated using $\sigma_d = 2.3$ m^2 g^{-1} and $\beta_d = 0.29$, while an upper value of $\Delta\widetilde{F_R}$, representative for wet aerosol particles, can be estimated using $\sigma_w = 4.7$ m^2 g^{-1} and $\beta_w = 0.17$. The use of σ_w and β_w leads practically to the same $\Delta\widetilde{F_R}$ as estimated with the central values of σ and β, while $\Delta\widetilde{F_R}$ becomes only 20% smaller when using σ_d and β_d. For that reason, we utilise in the following calculation of the local DE the central values for σ and β (Table 1) which are appropriate for usual ambient humidity.

2.3. Indirect sulphate aerosol effects

Sulphate aerosols affect the microphysical properties of clouds which can be expressed in terms of changes in the cloud optical thickness (first indirect effect, FIE) and changes in the lifetime of clouds (second indirect effect, SIE). The emission of sulphur involves an increase in the number of sulphate aerosol particles in clouds and thus an increase in the number of cloud condensation nuclei (CCN). The consequence of seeding a cloud with CCN is a decrease in the effective radius of the cloud droplets. A common assumption is that the decrease in the droplet radius is a process during which the liquid-water content of the clouds and the geometric thickness of the clouds hardly change (Twomey, 1974). Thus, FIE can be described to a first approximation by an increase in the cloud optical thickness. In addition, the decrease in the effective radius of the cloud droplets causes a decrease in the rate of autoconversion (Albrecht, 1989). In consequence, the formation of precipitation is inhibited, which prolongs the cloud lifetime. Thus, SIE can be described by an increased characteristic time of the rain drop formation. This leads to an increase in the cloud fraction, provided the other cloud processes as well as the advective and turbulent motions are retained.

A simulation of the indirect effects is accompanied with large uncertainties due to a still incomplete understanding of the contributing processes. Based on the current knowledge, a reasonable way to account for FIE and SIE due to sulphate aerosol burdens in CLIMBER-2 is to modify the optical thickness of clouds, and the characteristic turnover time of the precipitable liquid water of clouds, respectively. To modify these parameters in dependence of the sulphate aerosol burden, we use a simple scheme to transform the sulphate mass burden into a number concentration of sulphate aerosol particles which is further transformed into a number concentration of cloud droplets.

The determination of FIE is based on the definition of the short-wave optical thickness δ_c of liquid-water clouds

$$\delta_c = \frac{3\, w_0\, H_c}{2\, \rho_w\, r_c}, \tag{7}$$

where w_0 is the cloud liquid-water content (kg m^{-3}), H_c is the cloud geometric thickness, ρ_w is the water density, and r_c is the effective radius of cloud droplets (e.g. Liou, 2002). The determination of r_c depends mainly on w_0 and the number concentration of cloud droplets N_c

$$r_c = \left(\frac{3\, w_0}{4\pi\, \rho_w\, \kappa\, N_c}\right)^{1/3}, \tag{8}$$

where $\kappa = 0.67$ in continental air masses and $\kappa = 0.8$ in maritime air masses (Jones et al., 1994; Martin et al., 1994). Based on the assumption that w_0 and H_c remain unchanged when clouds are seeded with CCN, eqs (7) and (8) show that δ_c is proportional to the third root of the cloud droplet number concentration

$$\delta_c(N_c) \propto (N_c)^{1/3}. \tag{9}$$

In turn, N_c depends on the CCN number concentration, N_a, at the cloud base

$$N_c(N_a) = N_{c,0}\,[1 - \exp\{-\alpha_c\, N_a\}], \tag{10}$$

where the empirical coefficients are $N_{c,0} = 375 \times 10^6$ m^{-3} and $\alpha_c = 2.5 \times 10^{-9}$ m^3 (Jones et al., 1994). Alternative relationships for $N_c(N_a)$ as discussed in Jones et al. (2001) are found to cause relatively small differences in the present coarse scale applications. The CCN number concentration N_a consists of the natural CCN concentration N_a^{nat} and the anthropogenic sulphate aerosol concentration N_a^{ant} at the cloud base. Combining eqs (9) and (10)

shows that the emission of anthropogenic sulphate aerosols results in a modified cloud optical thickness

$$\delta_c(N_a) = \delta_c\left(N_a^{\text{nat}}\right)\,[f_{\text{mod}}]^{1/3}, \tag{11}$$

where $\delta_c(N_a^{\text{nat}})$ is the cloud optical thickness computed in CLIMBER-2 using a background concentration N_a^{nat} of natural CCN and f_{mod} is given by

$$f_{\text{mod}} = \frac{1 - \exp\{-\alpha_c N_a\}}{1 - \exp\left\{-\alpha_c N_a^{\text{nat}}\right\}}. \tag{12}$$

Since natural CCN consist mainly of sulphate aerosol particles, we consider N_a^{nat} to represent a background concentration of natural sulphate aerosols. A mean value of $N_a^{\text{nat}} = 75 \times 10^6$ m^{-3} was determined for pre-industrial times at the cloud base by Jones et al. (1994). The value of N_a^{nat} is difficult to assess but the value is compatible with the approximate minimum aerosol number concentration of 100×10^6 m^{-3} at the surface (Kiehl et al., 2000) and of 80×10^6 m^{-3} below marine clouds (Twohy et al., 2005).

The anthropogenic sulphate aerosol concentration at the cloud base N_a^{ant} can be determined by assuming that the sulphate aerosol number concentration decreases exponentially with height. Thus, N_a consisting of anthropogenic and natural sulphate aerosols at the cloud base is

$$N_a = N_a^{\text{ant}}(0)\,\exp\{-H_{st}/H_a\} + N_a^{\text{nat}}, \tag{13}$$

where N_a^{ant} (0) is the anthropogenic sulphate aerosol number concentration at the surface, H_a is the aerosol scale height, and H_{st} is the effective height of the cloud base. We prescribe $H_a =$ 1500 m analogous to the scale height of the specific humidity in CLIMBER-2, while H_{st} is a prognostic variable in the cloud scheme (Petoukhov et al., 2000). The value of $N_a^{\text{ant}}(0)$ follows directly from

$$N_a^{\text{ant}}(0) = L_a^{\text{ant}}/H_a, \tag{14}$$

where L_a^{ant} is the column-integrated anthropogenic aerosol number burden (m^{-2}). The value of L_a^{ant} can be inferred from the column-integrated sulphate aerosol mass burden B

$$L_a^{\text{ant}} = \frac{B}{\rho_a\, 4/3\,\pi\, r_a^3}, \tag{15}$$

where $\rho_a = 1.769 \times 10^6$ g m^{-3} is the density of sulphate aerosols and r_a is the effective radius of sulphate aerosol particles.

Under the ideal assumption that all climate variables are retained, eqs (12)–(15) yield $f_{\text{mod}} = 1.21$, by use of $B_G =$ 2.8 mg(SO$_4$) m^{-2}, $H_{st} = 4000$ m, $r_a = 0.1$ μm, and the above empirical values for N_a^{nat}, α_c and H_a. According to eq. (11) this implies an increase of the global mean cloud optical thickness by about 6%. We note that the sulphate aerosol radius increases with relative humidity in the atmosphere (see discussion in Section 2.2). Considering of the aerosol size distribution in polluted regions, r_a of sulphate aerosols ranges typically between 0.1 and 0.2 μm (Randriamiarisoa et al., 2006). Repeating the above calculation of f_{mod} using a 50% larger effective radius, that is, $r_a =$ 0.15 μm, leads to $f_{\text{mod}} = 1.09$ which implies an increase of δ_c by 2% only.

The determination of SIE is based on a theoretical relationship for the precipitation rate (Petoukhov, 1991; Liou, 1992). With the conventional assumption that the precipitation rate P in stratus and cumulus clouds depends primarily on the autoconversion process from small to large cloud droplets, P increases with cloud thickness and decreases with the number concentration of cloud droplets

$$P \propto (H_c)^{m+n/3}\,(N_c)^{-n/3}, \tag{16}$$

where $m \approx 1$ and $n \approx 3$. If we again assume that H_c remains constant when seeding clouds with sulphate aerosols, eq. (16) reduces to

$$P \propto (N_c)^{-1}. \tag{17}$$

Thus the modified precipitation rate due to seeding clouds with anthropogenic sulphate aerosols can be described by

$$P(N_a) = P\left(N_a^{\text{nat}}\right)/f_{\text{mod}}, \tag{18}$$

where $P(N_a^{\text{nat}})$ is the precipitation rate calculated in accord with the scheme of the hydrological cycle under a background concentration of natural aerosols and f_{mod} is defined by eq. (12). According to eq. (8) and under the same assumptions as before, SIE would yield a reduced global mean precipitation of 9–21% by use of $B_G = 2.8$ mg(SO$_4$) m^{-2}. We note that the actual precipitation change is computed consistently with the distributions of temperature and specific humidity.

2.4. Transient simulations

The modifications in the short-wave radiation scheme and in the cloud and precipitation scheme of CLIMBER-2 are tested in a series of simulations using the space–time varying sulphur emissions over 1850–2000 AD. The initial condition of all transient simulations is the equilibrium state of the CLIMBER-2 model driven with the $^{\text{eq}}CO_2$ concentration corresponding to the initial year 1850, that is, $C_c = 287.3$ ppm. The sulphate aerosol effects in this study are computed with the use of the effective parameter values (Table 1). Different simulations are conducted to account for the three aerosol effects separately or in combination, which is indicated in the name of simulation A by three lower indices (Table 2). The first, second and third lower indices at A correspond to the aerosol effects, respectively, DE, FIE and SIE. The lower index is 1 if the corresponding effect is accounted for, and 0 if it is not.

The simulations are divided in two subsets with (i) fixed greenhouse gas concentration (C_c) and (ii) growing greenhouse gas concentrations (C_e). The first subset of simulations is conducted to test the sensitivity of the radiative effects to the effective paramter values. The radiative effects due to the indirect aerosol

Table 2. Notation of transient simulations over 1850–2000 AD with different combinations of direct effect (DE), first indirect effect (FIE), and second indirect effect (SIE) using two different effective radii r_a, under constant or growing greenhouse gas concentrations

Simulation	Greenhouse gas conc.	Aerosol effect DE FIE SIE	r_a (μm)
$A_{100}C_c$	const.	1 0 0	[a]
$A^r_{110}C_c$	const.	1 1 0	0.10
$A^r_{111}C_c$	const.	1 1 1	0.10
$A_{110}C_c$	const.	1 1 0	0.15
$A_{111}C_c$	const.	1 1 1	0.15
$A_{100}C_e$	grow.	1 0 0	[a]
$A_{110}C_e$	grow.	1 1 0	0.15
$A_{111}C_e$	grow.	1 1 1	0.15
C_e	grow.	0 0 0	–

[a]The direct aerosol effect is only implicitly influenced by r_a (see discussion in Section 2.2).

Table 3. Shortwave radiative forcing ΔF_R due to combinations of sulphate aerosol effects for the anthropogenic sulphur emission in 2000 given as global, NH and SH means using two different effective radii r_a of sulphate aerosols and $^{eq}CO_2$ concentration of 1850

Simulation	ΔF_R (W m^{-2})	ΔF_R^{NH} (W m^{-2})	ΔF_R^{SH} (W m^{-2})	$\frac{\Delta F_R^{NH}}{\Delta F_R^{SH}}$	r_a (μm)
$A_{100}C_c$	−0.41	−0.71	−0.10	7.1	–
$A^r_{010}C_c$	−1.03	−1.70	−0.37	4.6	0.10
$A^r_{001}C_c$	−1.15[a]	−1.66[a]	−0.63[a]	2.6	0.10
$A^r_{110}C_c$	−1.42	−2.37	−0.47	5.1	0.10
$A^r_{111}C_c$	−1.44[a]	−2.41[a]	−0.48[a]	5.1	0.10
$A_{010}C_c$	−0.42	−0.71	−0.12	5.9	0.15
$A_{001}C_c$	−0.48[a]	−0.73[a]	−0.23[a]	3.2	0.15
$A_{110}C_c$	−0.81	−1.41	−0.22	6.4	0.15
$A_{111}C_c$	−0.81[a]	−1.40[a]	−0.22[a]	6.3	0.15

[a]Radiative forcing of SIE is an approximate value from the change in short-wave radiation at TOA since climate variables are not kept fixed.

forcing of FIE and SIE are found to be very sensitive to the effective radius of the sulphate aerosols (Section 2.3). This is demonstrated by displaying the radiative effects obtained for two values, $r_a = 0.10$ and $0.15\,\mu$m. The usage of $r_a = 0.1\,\mu$m is marked in the name A by the upper index r (Table 2). The second subset of simulations serves to study the interplay of the effects from the sulphate aerosol and the greenhouse gas forcing. Finally, the simulation C_e is performed with growing $^{eq}CO_2$ concentration and without aerosol effects to compare individual climatic responses.

3. Results

3.1. Radiative forcing from sulphate aerosol burden in 2000

The short-wave radiative forcing of sulphate aerosols is calculated via the instantaneous change in the short-wave radiation at TOA due to seeding sulphate aerosols into the lower troposphere while holding the surface and tropospheric temperatures and the other climate variables fixed. Thus the global and annual mean radiative forcing due to the direct sulphate aerosol effect is comparable with $\Delta\widetilde{F_R}$ in eq. (2). (Henceforth, we omit $\widetilde{\cdot}$ for global and annual means.) Also, the short-wave radiative forcing of FIE through changing the cloud optical thickness can be calculated by holding all other climate variables fixed. In contrast, the radiative forcing attributed to SIE represents an approximate value since a change in the cloud lifetime involves changes in cloud fraction and atmospheric temperature.

Table 3 shows the global and hemispheric short-wave radiative forcing caused by the anthropogenic sulphur dioxide emissions in 2000. In the global and annual mean, the radiative forcing of the direct effect is $\Delta F_R = -0.41$ W m^{-2} which is in the range of the direct radiative forcing given in IPCC (2001), and in the range from -0.16 to -0.58 W m^{-2} given in Schulz et al. (2006). In 2000, the ratio of the anthropogenic burden of sulphate aerosols from NH and SH is 8.1, and the ratio of the direct radiative forcing in NH and SH is $\Delta F_R^{NH}/\Delta F_R^{SH} = 7.1$ in simulation $A_{100}C_c$. This ratio of the hemispheric radiative forcing is at the upper edge of the range of values compiled by the IPCC (2001). Ratios of the hemispheric radiative forcing from simulations including FIE and SIE tend to become smaller than the ratio from including only DE.

The annual mean pattern of the direct radiative forcing resembles the pattern of sulphate aerosol burden (compare Figs. 3a and 2b). Nevertheless, the aerosol burden, which is constant over the year, involves a seasonally changing direct radiative forcing due to the seasonal changes in insolation, surface albedo and cloudiness. Hence, the radiative forcing which is concentrated over the areas of main sulphur dioxide emissions in North America, Europe and Southeast Asia is about twice as strong in the boreal summer months (JJA, Fig. 3c) than in the boreal winter months (DJF, Fig. 3b).

3.2. Climatic responses to sulphate aerosol burden over 1850–2000

The responses of the climate variables to the year-to-year varying sulphur dioxide emissions (Section 2.1), which modify the combined surface–aerosol albedo (Section 2.2), the cloud optical thickness and the turnover time of cloud water (Section 2.3) are displayed as global and annual means in Fig. 4. The sulphate aerosol albedo a_a (eq. 6) grows uniformly in all simulations up to about 0.005 (Fig. 4a). In 2000, the relative increase in surface albedo a_s with respect to a_s of 1850 is 0.5, 1.3 and 2.4% obtained in the simulations $A_{100}C_c$, $A_{110}C_c$ and $A_{111}C_c$, respectively

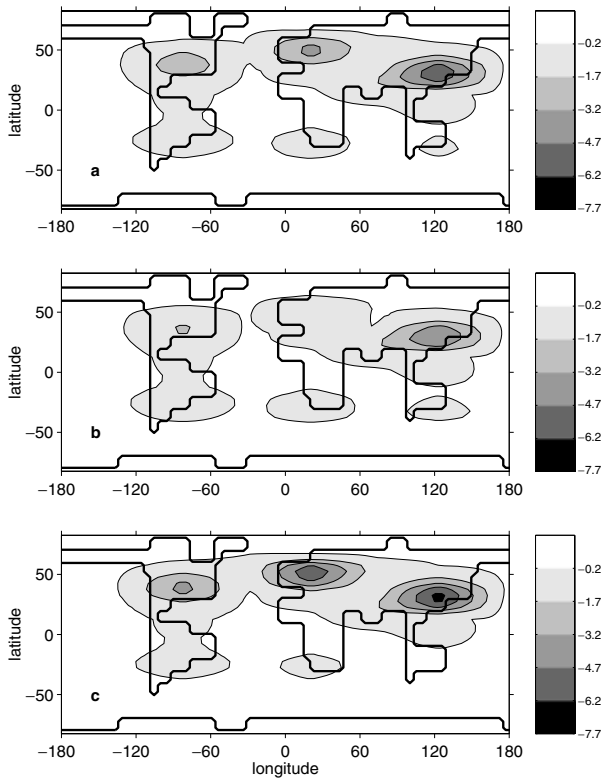

Fig. 3. Horizontal distribution of the direct radiative forcing ΔF_R (W m^{-2}) due to sulphate aerosol burden in 2000 (see Fig. 2b) shown for (a) annual mean, (b) DJF and (c) JJA from simulation $A_{100}C_c$.

(Fig. 4b). The increase in a_s is connected with an increase of the sea ice area and the snow coverage. The combined surface–aerosol albedo a_{sa} (eq. 5) shows in 2000, relative to 1850, increases of 2.3, 3.1 and 4.1% in the simulations $A_{100}C_c$, $A_{110}C_c$ and $A_{111}C_c$, respectively (Fig. 4c).

Increases in a_s and a_{sa} involve increases in the planetary albedo (Fig. 4d) whereby the absorbed insolation at TOA, $F = S_0(1 - a_p)/4$, decreases (Fig. 4e). The change in the absorbed insolation consists primarily of the aerosol-induced direct radiative forcing and is amplified by radiative contributions from induced increases in surface albedo and cloud albedo. For instance in simulation $A_{100}C_c$, the direct radiative forcing is $\Delta F_R = -0.41$ W m^{-2} while the decrease in insolation is $\Delta F = -0.52$ W m^{-2} as a result of positive feedback processes. The climatic response, which incorporates the feedback processes, is characterised by a decrease in surface air temperature (Fig. 4f), an increase in cloud fraction (Fig. 4g) and a decrease in precipitation rate (Fig. 4h). The cooling through DE in simulation $A_{100}C_c$ involves a relatively small increase in cloud fraction (0.1%) and a relatively small decrease in precipitation rate (−0.8%). In simulation $A_{110}C_c$, DE and FIE produce also small relative changes in cloud fraction (0.2%) and precipitation rate (−1.3%), but in simulation $A_{111}C_c$, all aerosol effects together involve significant changes in cloud fraction (0.8%) and precipitation rate (−3.2%). The cooling associated with SIE is a minor implication of the increase in cloud lifetime.

3.3. Climatic responses to sulphate aerosols and greenhouse gases

3.3.1. Global and hemispheric means. The individual sulphate aerosol effects lead at the end of the 150 year-long simulations to cooler global temperatures by −0.17, − 0.18 and −0.07 K in the simulations $A_{100}C_c$, $A_{010}C_c$ and $A_{001}C_c$, respectively. The $^{eq}CO_2$-driven simulation C_e leads to a warming of the global temperature by 1.0 K. The $^{eq}CO_2$-induced global warming declines successively through the activation of the sulphate aerosol effects in the simulations $A_{100}C_e$ (0.84 K), $A_{110}C_e$ (0.68 K) and $A_{111}C_e$ (0.59 K). The sum of the individual temperature changes is seen to agree closely with the temperature response to all effects in simulation $A_{111}C_e$ (Table 4).

The aerosol-induced cooling is always larger in NH than in SH with the ratio $\Delta T^{NH}/\Delta T^{SH} \approx 2.5$, irrespective of the activated aerosol effect. The $^{eq}CO_2$-induced warming is larger in NH (1.16 K) than in SH (0.84 K). Although the aerosol-induced cooling is larger in NH than in SH, in the simulation $A_{100}C_e$ the NH warming (0.91 K) exceeds the SH warming (0.76 K). Only the activation of FIE and SIE in $A_{110}C_e$ and $A_{111}C_e$ leads to less warming in NH than in SH. The apparent linearity in the temperature response to different types of forcing can also be seen for the hemispheric temperatures. However, the ratio $\Delta T^{NH}/\Delta T^{SH}$ in $A_{100}C_c$ (Table 4) is at least a factor two smaller than the corresponding ratio of the direct radiative forcing (Table 3) indicating that the hemispheric response to the different direct radiative forcing in NH and SH is partially compensated by internal processes. These processes comprise interhemispheric exchanges of sensible and latent heat due to the Hadley cell circulation and the macroturbulence associated with synoptic scale eddies/waves (Peixoto and Oort, 1992) and also exchanges by the oceanic transport; although the latter two contributions are less important than the Hadley cell circulation.

The global and annual mean precipitation changes are seen to be correlated with the temperature changes (Table 4). The cooling in the aerosol-driven simulations is accompanied with less precipitation reaching up to −3.4% in simulation $A_{111}C_c$. The warming in simulation C_e is associated with an increased precipitation rate (4%), and the dominance of the $^{eq}CO_2$-induced warming over the aerosol-induced cooling leads to an increased precipitation rate (0.5%) in the simulation $A_{111}C_e$. However, the NH decrease in the precipitation rate (−1%) in simulation $A_{111}C_e$ shows that the aerosol-induced precipitation decrease overcompensates the $^{eq}CO_2$-induced precipitation increase.

The correlation between precipitation rate and temperature can be expressed by the hydrological sensitivity. The simulations accounting for DE, FIE or the $^{eq}CO_2$ concentration yield $\Delta P/\Delta T \approx 4$%/K (Table 4). That value agrees closely with 3.9%/K in Feichter et al. (2004) from the aerosol-driven simulation but

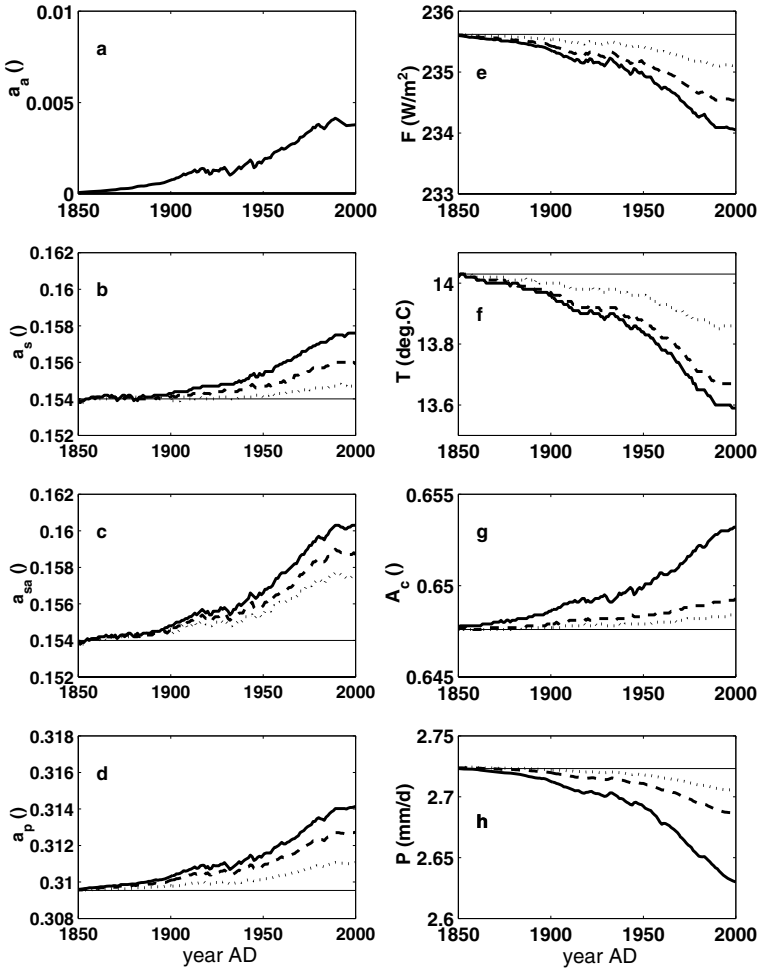

Fig. 4. Time series over 1850–2000 from simulations (see Table 2) $A_{100}C_c$ (dotted), $A_{110}C_c$ (dashed) and $A_{111}C_c$ (continuous) showing global and annual means of (a) aerosol albedo a_a, (b) surface albedo a_s, (c) combined surface–aerosol albedo a_{sa}, (d) planetary albedo a_p, (e) absorbed short-wave radiation at TOA F (W m^{-2}), (f) surface air temperature T (°C), (g) cloud fraction A_c and (h) precipitation rate P (mm d^{-1}). Thin straight lines mark initial value in 1850.

Table 4. Changes in surface air temperature ΔT in K and precipitation rate ΔP in % in 2000 relative to 1850 as global, NH and SH means. The precipitation changes are normalised by the precipitation rate in 1850 of 2.72, 2.67 and 2.78 mm d^{-1} for the global, NH and SH mean, respectively

Simulation	ΔT (K)	ΔT^{NH} (K)	ΔT^{SH} (K)	ΔP (%)	ΔP^{NH} (%)	ΔP^{SH} (%)	$\frac{\Delta P}{\Delta T}$ (%/K)
$A_{100}C_c$	−0.17	−0.25	−0.10	−0.7	−1.1	−0.3	4.0
$A_{010}C_c$	−0.18	−0.26	−0.11	−0.7	−1.0	−0.4	3.7
$A_{001}C_c$	−0.07	−0.10	−0.04	−2.1	−3.5	−0.7	[a]
$A_{110}C_c$	−0.35	−0.52	−0.19	−1.4	−2.1	−0.7	3.9
$A_{111}C_c$	−0.43	−0.62	−0.23	−3.4	−5.5	−1.4	8.0
$A_{100}C_e$	0.84	0.91	0.76	3.3	3.7	2.9	3.9
$A_{010}C_e$	0.84	0.91	0.77	3.3	3.8	2.9	3.9
$A_{001}C_e$	0.94	1.05	0.82	1.8	1.2	2.5	1.9
$A_{110}C_e$	0.68	0.66	0.70	2.6	2.7	2.6	3.8
$A_{111}C_e$	0.59	0.53	0.65	0.5	−1.0	1.9	0.8
C_e	1.00	1.16	0.84	4.0	4.9	3.2	4.0

[a]The determination of $\Delta P/\Delta T$ from simulation with SIE has little meaning as SIE involves a change in P while the change in T is minor.

overestimates the value of 1.5%/K in Feichter et al. (2004) from the greenhouse-gas simulation. We note, however, that the study by Feichter et al. (2004) includes additional aerosol effects from black carbon and particulate organic matter which precludes a further analysis of the differences in the hydrological sensitivity.

3.3.2. Zonal means for winter and summer. The seasonal responses of climate system variables to the spatially varying sulphate aerosol burden and the homogeneous $^{\mathrm{eq}}CO_2$ concentration are exhibited by zonal mean changes for DJF (Fig. 5) and JJA (Fig. 6). The changes are calculated by subtracting zonal means of 1850 from zonal means of 2000 and the relative changes are given with respect to the zonal mean of 1850. The zonal mean changes are shown from simulations $A_{111}C_c$, C_e and $A_{111}C_e$.

The regionally limited sulphate aerosol burden (Figs. 5a and 6a) causes a global cooling in $A_{111}C_c$, which exceeds 1 K north of 60°N in DJF (Fig. 5b) and also at 40–70°N in JJA (Fig. 6b). The $^{\mathrm{eq}}CO_2$-induced warming overcompensates the aerosol-induced cooling, and $A_{111}C_e$ yields a warming of more than 1 K north of 70°N during DJF, and a larger warming in SH than in NH during JJA. The precipitation rate reduces globally in $A_{111}C_c$ through the

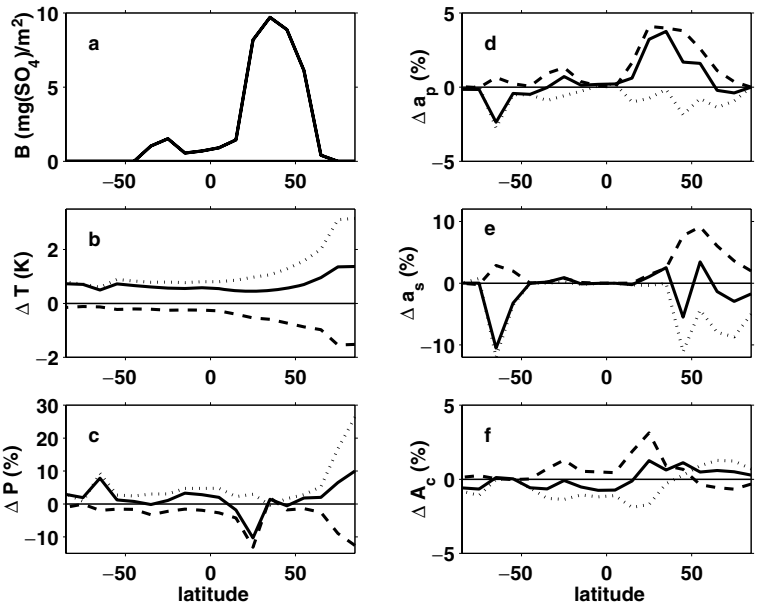

Fig. 5. Zonal means for DJF from simulations $A_{111}C_c$ (dashed), C_e (dotted) and $A_{111}C_e$ (continuous). Panels show (a) mass burden of sulphate aerosols B [mg(SO_4) m^{-2}] in year 2000 and (b) surface air temperature change ΔT (K) in 2000 relative to 1850, and panels (c)–(f) show relative changes from 1850 to 2000 by normalisation with mean of 1850 for (c) precipitation ΔP (%), (d) planetary albedo Δa_p (%), (e) surface albedo Δa_s (%) and (f) cloud fraction ΔA_c (%).

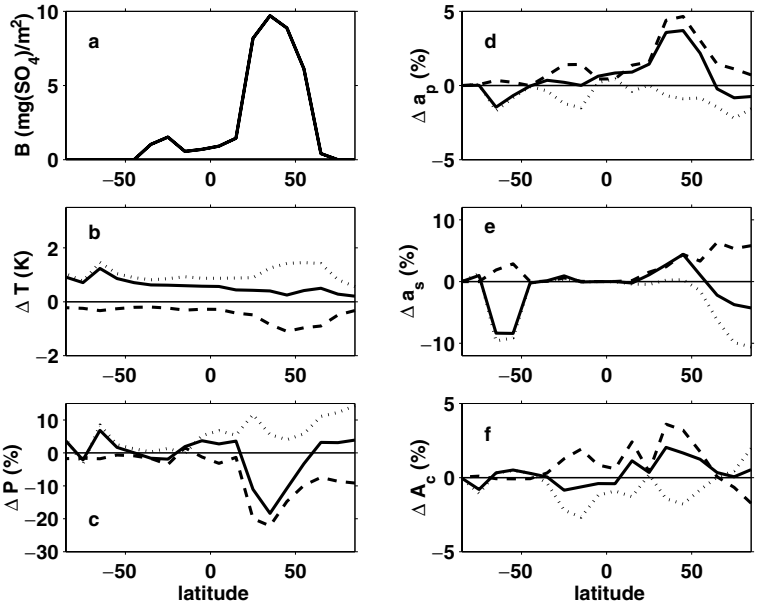

Fig. 6. As Fig. 5 but for JJA; note different range of relative precipitation change in (c).

aerosol effects. During DJF, the relative change in precipitation rate is about −10% at 20–30°N and north of 80°N (Fig. 5c), and reaches about −20% at 20–40°N in JJA (Fig. 6c). The $^{eq}CO_2$-induced change in precipitation is positive everywhere. In total, the simulation $A_{111}C_e$ yields latitudinally varying rain changes. These zonal mean changes are positive in SH and in the tropical latitudes, negative in the northern subtropical and mid latitudes, and again positive in the high northern latitudes in both seasons.

The planetary albedo in simulation $A_{111}C_c$ is seen to increase by more than 4% in the latitudes of main sulphate aerosol burden in both seasons (Figs. 5d and 6d). The increase in the planetary albedo outweighs the relatively small decrease in planetary albedo connected with the $^{eq}CO_2$ forcing. In contrast, the surface albedo changes mainly in latitudes with snow and ice cover (Figs. 5e and 6e). The relative changes in a_s in $A_{111}C_c$ approach 9% at 50–60°N during DJF and 6% north of 60°N during JJA. The changes in a_s in simulation C_e are about −10% at 60–70°S and north of 70°N. Thus in $A_{111}C_e$, a_s decreases around Antarctica up to 8% during DJF and JJA because the $^{eq}CO_2$-induced warming effect overcompensates the aerosol-induced cooling effect, while a_s varies in NH between ±5% in both seasons. The relative changes in cloud fraction show latitudinal variations of inverse sign from the aerosol forcing and the $^{eq}CO_2$ forcing in both seasons (Figs. 5f and 6f). The total effect on cloud fraction

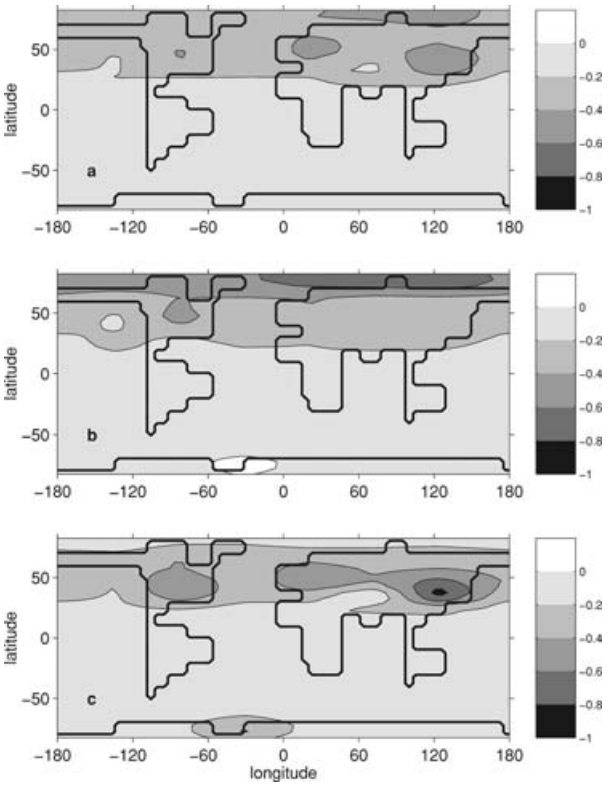

Fig. 7. As Fig. 3 but for surface air temperature response ΔT (K) from simulation $A_{100}C_c$.

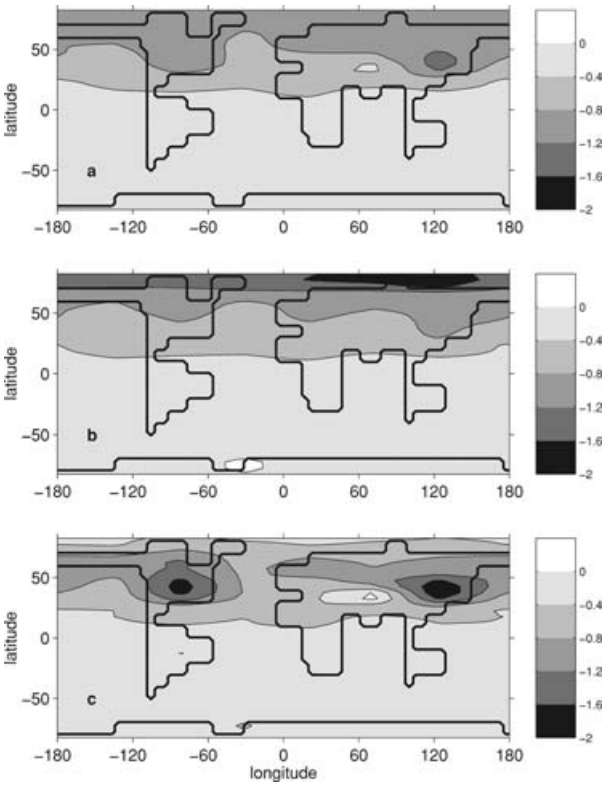

Fig. 8. As Fig. 3 but for surface air temperature response ΔT (K) from simulation $A_{111}C_c$.

in $A_{111}C_e$ is a weak decrease in tropical latitudes and a weak increase in subtropical and northern mid-latitudes.

3.3.3. Response patterns for winter and summer. Annual mean geographical patterns of climatic responses to the different anthropogenic factors can deviate significantly from the seasonal response patterns of DJF and JJA. This is shown by the response patterns in Figs. 7–13 which are obtained by subtracting the horizontal climate fields of 1850 from the climate fields of 2000.

Figure 7 shows the response patterns of the surface air temperature calculated with the direct radiative forcing (Fig. 3) in simulation $A_{100}C_c$. The temperature decreases globally but mainly north of 30°N. The annual cooling is around −0.5 K over Southeast Asia, Europe, the Asian Arctic sector, and North America (Fig. 7a). During DJF (Fig. 7b), the maximum cooling approaches −0.8 K in the northern polar latitudes. The polar cooling is a consequence of the sea-ice albedo feedback through which the aerosol-induced cooling is amplified by less melting of sea-ice during JJA. This involves a larger surface albedo and less warming in JJA of the upper ocean, followed by a stronger cooling of the air temperature during DJF due to a reduced heat flux to the northern lower atmosphere. During JJA (Fig. 7c), the cooling pattern is similar to the pattern of the direct sulphate aerosol forcing (Fig. 3c), as the largest cooling occurs over Southeast Asia (about −0.8 K) and secondary cooling maxima occur over Europe and North America.

The cooling patterns due to DE in $A_{100}C_c$ (Fig. 7) and due to all aerosol effects in $A_{111}C_c$ (Fig. 8) are similar but the cooling in $A_{111}C_c$ is twice as large as in $A_{100}C_c$. The aerosol effects in $A_{111}C_c$ cause a reduced precipitation rate (Figs. 9a–c) in the areas of negative radiative forcing. The patterns of ΔP in $A_{111}C_c$ closely resemble ΔP in $A_{100}C_c$ (not shown) but the former anomalies are four times as large as the latter. The precipitation rate reduces mainly during JJA in the Asian summer monsoon area (−2.5 mm d^{-1}), and is about −1 mm d^{-1} over Europe and the southern North America.

The simulation C_e produces a latitudinal varying warming (Fig. 10). The annual mean warming is 0.6–1.2 K south of about 40°N and increases northward to more than 2 K (Fig. 10a). The largest warming of more than 3 K occurs during DJF in the northern high latitudes (Fig. 10b), amounts to 1.2–1.8 K in JJA in the northern mid-latitudes (Fig. 10c) and is larger over northern land areas than over ocean areas. The $^{eq}CO_2$-induced warming leads to a decrease of the northern sea-ice area during JJA and a warming of the upper ocean (sea-ice albedo feedback) involving an enhanced heat flux to the northern lower atmosphere during DJF. The response pattern of ΔP in C_e is positive in the equatorial belt and reaches 0.4–0.6 mm d^{-1} in the Amazon region (Fig. 11a). During DJF, ΔP is positive in a belt south of the equator and is negative in the northern subtropical latitudes mainly over land areas (Fig. 11b). The largest increase in P of more than

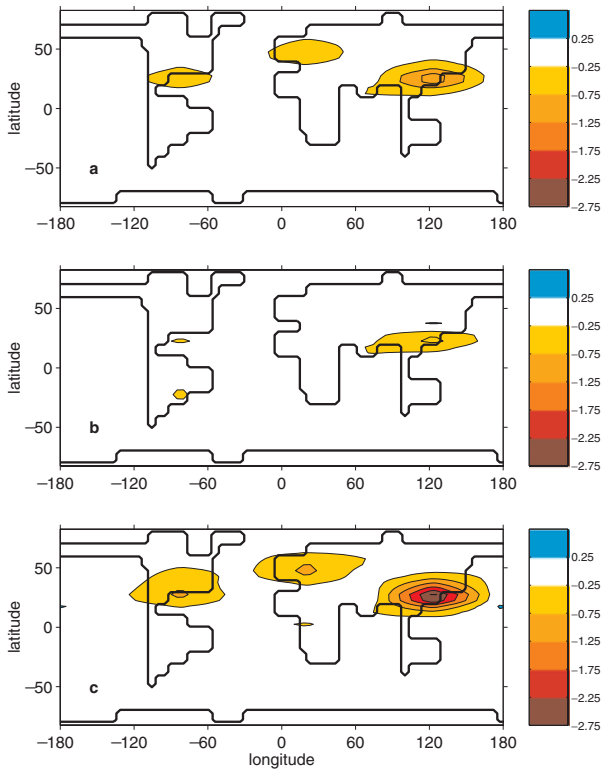

Fig. 9. As Fig. 3 but for precipitation response ΔP (mm d^{-1}) from simulation $A_{111}C_c$.

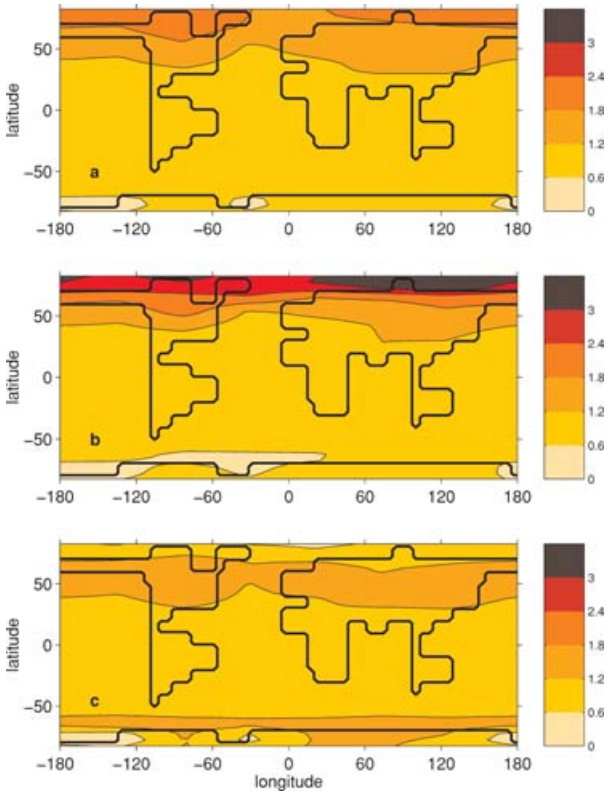

Fig. 10. As Fig. 3 but for surface air temperature response ΔT (K) from simulation C_e.

0.6 mm d^{-1} occurs during the Asian summer monsoon (Fig. 11c). Secondary maxima in ΔP are seen in the Sahel zone, the Amazon area and in the southern North America during JJA.

The response to all effects in simulation $A_{111}C_e$ changes significantly from 1989 with maximum sulphur emissions to 2000 with maximum $^{eq}CO_2$ concentration. In 1989, the annual mean $^{eq}CO_2$-induced warming is about balanced by the aerosol-induced cooling over southern North America, North Atlantic and Southeast Asia while the temperature over Europe cools between −0.2 and −0.6 K (not shown). In 2000, the $^{eq}CO_2$-induced warming prevails globally over the aerosol-induced cooling (Fig. 12a). During DJF in 1989, the warming in the northern polar region approaches 1 K, while in 2000 the DJF warming exceeds 1.4 K (Fig. 12b). During JJA in 2000, the aerosol-induced cooling outweighs the $^{eq}CO_2$-induced warming only over North America and Southeast Asia (Fig. 12c), while the $^{eq}CO_2$-induced warming dominates in central Asia and in the SH, where the warming reaches 1–1.4 K around Antarctica.

The annual pattern of ΔP in 2000 (Fig. 13a) shows negative anomalies between −0.25 and −1.3 mm d^{-1} over the three major areas of sulphate aerosol burden, and positive anomalies above 0.25 mm d^{-1} over the Amazon area and the tropical western Pacific. During DJF, ΔP lies within ±0.75 mm d^{-1} (Fig. 13b) and lies between −2.75 and 0.75 mm d^{-1} during JJA (Fig. 13c). The effects of the sulphate aerosols and the $^{eq}CO_2$ concentration impose changes of inverse sign on the Asian summer monsoon whereby the inhomogeneous sulphate aerosol burden leads to a bimodal distribution with less rainfall (−2.5 mm d^{-1}) in Southeast Asia and more rainfall (0.5 mm d^{-1}) over India.

3.4. *Simulated and observed temperature changes over 1850–2000*

The annual mean temperature changes in response to the direct and indirect sulphate aerosol effects from anthropogenic emissions are relevant for reproducing observed temperature changes with climate models. Fig. 14 shows the temperature anomalies over 1850–2000 from observed data as global, NH and SH means (Brohan et al., 2006). The observed temperature anomalies with respect to the mean over 1850–1880 are compared with the simulated temperature responses in the simulations $A_{111}C_c$, C_e and $A_{111}C_e$. The simulated warming due to the growing $^{eq}CO_2$ concentration overestimates the observed warming in the last century while the temperature increase in the simulation $A_{111}C_e$ with sulphate aerosol and greenhouse gas effects leads to a considerably improved reproduction of the observed centennial warming trend.

The interannual and interdecadal variations are not resolved by the simulation since the contributions from volcanic and solar

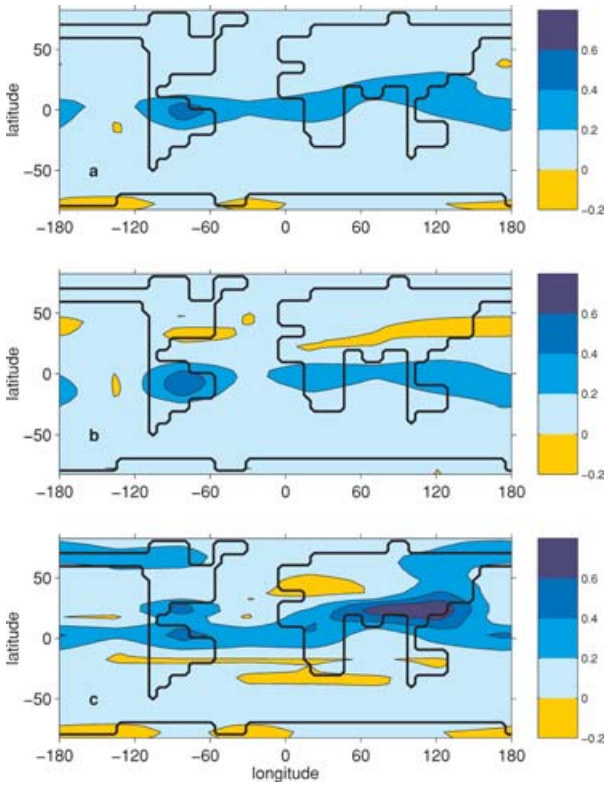

Fig. 11. As Fig. 3 but for precipitation response ΔP (mm d^{-1}) from simulation C_e.

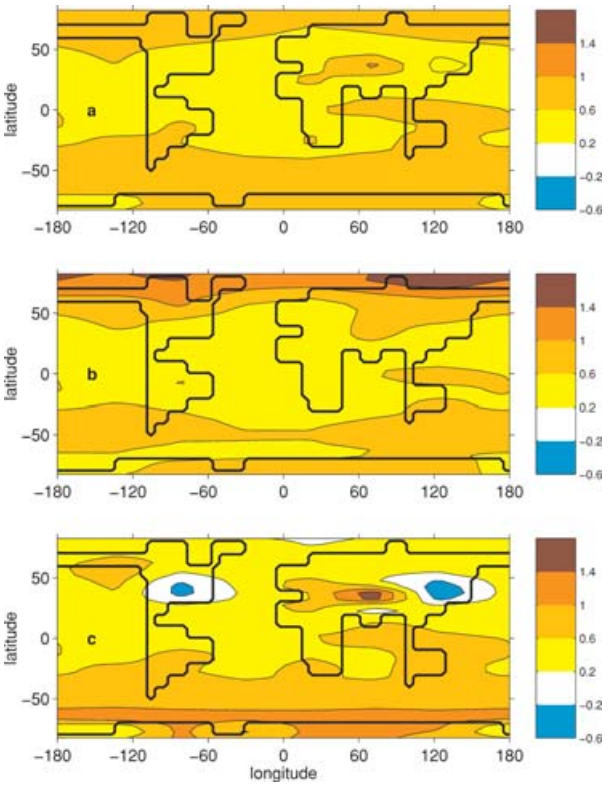

Fig. 12. As Fig. 3 but for surface air temperature response ΔT (K) from simulation $A_{111}C_e$.

activity and the interannual variability are ignored. Furthermore, the El Niño-Southern Oscillation and other intradecadal and interdecadal varying modes are not reproduced. The short-term variations in the observed temperature series exceed the interhemispheric differences largely which makes a more detailed analysis of hemispheric temperature changes difficult. Nonetheless, the seasonal temperature anomalies in simulation $A_{111}C_e$ reveal a larger NH warming during DJF (0.61 K) than during JJA (0.42 K) which is in line with the temperature reconstructions over 1861–2000 by Jones et al. (2003).

4. Conclusions

In the time interval 1850–2000 AD, the global climate changes are influenced by anthropogenic activity largely as a result of the progressive emissions of greenhouse gases and sulphur dioxide from fossil fuel burning. As a step toward improving the simulation of the past climate changes with the Earth system model CLIMBER-2, a physical based scheme for sulphate aerosol effects is presented with the goal to obtain a computational efficient climate system model suitable for investigations into future climate policy strategies. The computational efficiency is obtained by ignoring chemical and dynamical processes of the sulphur cycle which can be justified by the short lifetime of sulphate aerosols and the coarse spatial grid of the model. The proposed scheme concentrates on the calculation of the climatic impact induced by sulphate aerosols and neglects the influences of other aerosol components such as carbonaceous aerosols, mineral dust and sea salt.

The scheme is capable to account for localized emission data of sulphur dioxide and determines distributions of sulphate aerosol burdens by assuming an effective lifetime of sulphur aerosols. The sulphate aerosol effects are calculated in a physically consistent manner with the short-wave radiation scheme in CLIMBER-2. The calculation utilises a few effective parameters describing the physical and optical properties of sulphate aerosols (aerosol particle radius, scattering efficiency and upscatter fraction) and geophysical characteristics (atmospheric sulphate aerosol lifetime, scale height and natural aerosol concentration) in close relationship to measurements, theoretical Mie calculations and numerical GCM simulations. Each parameter has a range of uncertainty which can be attributed to aerosol composition, size distribution, relative humidity and wavelength. The values of the effective parameters are chosen from the centres of the uncertainty ranges related to the wavelength of 0.55 μm and to the usual ambient relative humidity. Simulations conducted with the described parameters show that the climatic responses compare reasonably well with analogous results from GCM simulations.

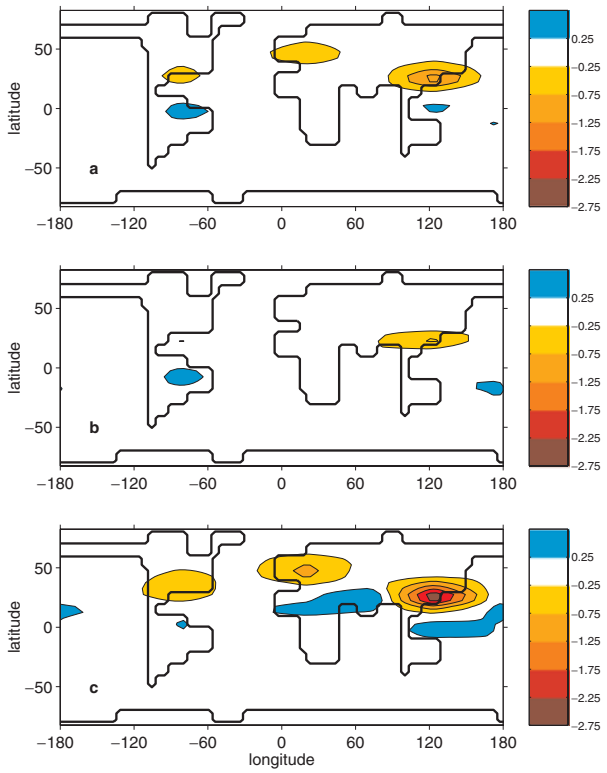

Fig. 13. As Fig. 3 but for precipitation response ΔP (mm d^{-1}) from simulation $A_{111}C_e$.

The calculated loading of anthropogenic sulphate aerosols over 1850–2000 agrees with the global mean loading in Boucher and Pham (2002) who used a sulphur cycle model and historical trends in emission data on a per country basis. In 2000, the anthropogenic sulphate aerosol loading reaches 0.47 TgS. The resulting best guess for the short-wave radiative forcing due to the direct sulphate aerosol effect is -0.4 W m^{-2} which is compatible with results in IPCC (2001) and Schulz et al. (2006). The best guess for the change in the short-wave radiation at TOA due to all sulphate aerosol effects is -0.8 W m^{-2}. This radiative effect including the direct, the first and second indirect effects can only be compared with model simulations and appears comparable with results in Lohmann and Lesins (2002). The global temperature rise over 1850–2000 simulated with the growing $^{eq}CO_2$ concentration and the sulphate aerosol loading amounts to 0.6 K. This agrees with observational data (e.g. Brohan et al., 2006) showing that the natural climate variability is considerably influenced through effects from anthropogenic activity. Furthermore, the sulphate aerosol effects influence the hydrological cycle. The simulation which includes the second indirect effect suggests a decrease of the global hydrological sensitivity from 4 to 0.8%/K which is in line with findings by Feichter et al. (2004).

The regional and seasonal varying temperature response induced by the sulphate aerosol effects and greenhouse gases can differ significantly from the global and annual mean response. The sulphate aerosol effects involve a larger cooling in NH than in SH and the NH cooling is larger in JJA than in DJF. The difference in the seasonal temperature response is largely connected with the seasonal cycle of the insolation leading to the larger cooling in the northern mid-latitudes during JJA than during DJF. Since we apply in the model annual sulphate aerosol burdens, the indicated decrease in the seasonal temperature contrast represents rather a lower estimate. A larger decrease in the seasonal temperature contrast can be expected because chemistry-transport model simulations show higher sulphate aerosol burdens during JJA than during DJF due to the more effective

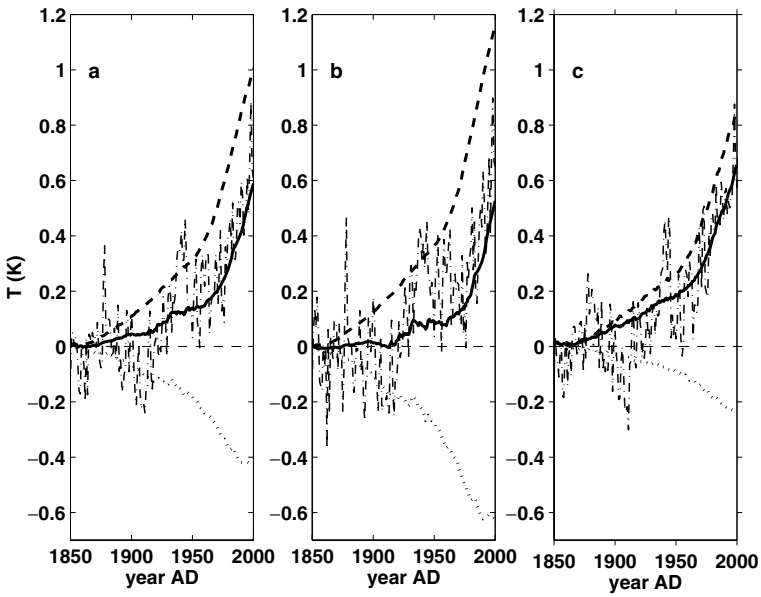

Fig. 14. Changes in annual surface air temperature (K) over 1850–2000 averaged for (a) globe, (b) NH and (c) SH from simulations $A_{111}C_c$ (dotted), C_e (dashed) and $A_{111}C_e$ (continuous) in comparison to HadCRUT3 data (dash–dotted).

oxidation of sulphur dioxide to sulphate aerosols in summer (Myhre et al., 2004). The cooling induced by the sulphate aerosol effects is enhanced in the model by the positive sea-ice albedo feedback which affects mainly the high northern latitudes. The simulated temperature response to the sulphate aerosol effects together with the greenhouse gas forcing agrees reasonably well with GCM simulations and observations on seasonal and large regional scales, which makes the CLIMBER-2 model a useful tool for investigating climate changes connected with future anthropogenic emission scenarios.

5. Acknowledgments

The authors thank Hermann Held and Elmar Kriegler for processing the aerosol emission data. Fortunat Joos kindly provided the data of greenhouse gas concentrations. Discussions with Johann Feichter and the ENIGMA group are greatly appreciated. EB acknowledges support partly by DFG grant CL/178 3-2 and VW grant II/78470. AE was partly funded by the Russian President grant 4166.2006.5 and by the Russian Foundation for Basic Research (project 07-05-00273). The authors are also thankful to the valuable comments of two anonymous reviewers.

References

Albrecht, B. A. 1989. Aerosols, cloud microphysics, and fractional cloudiness. *Science* **245**, 1227–1230.

Bauer, E., Claussen, M., Brovkin, V. and Huenerbein, A. 2003. Assessing climate forcings of the Earth system for the past millennium. *Geophys. Res. Lett.* **30**, 1276, doi:10.1029/2002GL016639.

Bauer, E. and Claussen, M. 2006. Analyzing seasonal temperature trends in forced climate simulations of the past millennium. *Geophys. Res. Lett.* **33**, L02702, doi:10.1029/2005GL024593.

Boucher, O., Schwartz, S. E., Ackerman, T. P., Anderson, T. L., Bergstrom, B. and co-authors. 1998. Intercomparison of models representing direct shortwave radiative forcing by sulfate aerosols. *J. Geophys. Res.* **103**, 16979–16998.

Boucher, O. and Pham, M. 2002. History of sulfate aerosol radiative forcings. *Geophys. Res. Lett.* **29**, 1308, 10.1029/2001GL014048.

Brohan, P., Kennedy, J. J., Harris, I., Tett, S. F. B. and Jones, P. D. 2006. Uncertainty estimates in regional and global observed temperature changes: a new data set from 1850. *J. Geophys. Res.* **111**, D12106, doi:10.1029/2005JD006548.

Brovkin, V., Bendtsen, J., Claussen, M., Ganopolski, A., Kubatzki, C. and co-authors. 2002. Carbon cycle, vegetation and climate dynamics in the Holocene: experiments with the CLIMBER-2 model. *Global Biogeochem. Cycles* **16**, 1139, doi:10.1029/2001GB001662.

Charlson, R. J., Langner, J., Rodhe, H., Leovy, C. B. and Warren, S. G. 1991. Perturbation of the northern hemisphere radiative balance by backscattering from anthropogenic sulfate aerosols. *Tellus* **43AB**, 152–163.

Charlson, R. J., Schwartz, S. E., Hales, J. M., Cess, R. D., Coackley, J. A. and co-authors. 1992. Climate forcing by anthropogenic aerosols. *Science* **255**, 423–430.

Chuang, C. C., Penner, J. E., Taylor, K. E., Grossman, A. S. and Walton, J. J. 1997. An assessment of the radiative effects of anthropogenic sulfate. *J. Geophys. Res.* **102**, 3761–3778.

Chylek, P. and Wong, J. 1995. Effect of absorbing aerosols on global radiation budget. *Geophys. Res. Lett.* **22**, 929–931.

Claussen, M., Kubatzki, C., Brovkin, V., Ganopolski, A., Hoelzmann, P. and co-authors. 1999. Simulation of an abrupt change in Saharan vegetation at the end of the mid-Holocene. *Geophys. Res. Lett.* **24**, 2037–2040.

Crowley, T. J. 2000. Causes of climate change over the past 1000 years. *Science* **289**, 270–277.

Feichter, J., Lohmann, U. and Schult, I. 1997. The atmospheric sulfur cycle in ECHAM-4 and its impact on the shortwave radiation. *Clim. Dyn.* **13**, 235–246.

Feichter, J., Roeckner, E., Lohmann, U. and Liepert, B. 2004. Nonlinear aspects of the climate response to greenhouse gas and aerosol forcing. *J. Climate* **17**, 2384–2398.

Ganopolski, A., Rahmstorf, S., Petoukhov, V. and Claussen, M. 1998a. Simulation of modern and glacial climates with a coupled model of intermediate complexity. *Nature* **391**, 351–356.

Ganopolski, A., Kubatzki, C., Claussen, M., Brovkin, V. and Petoukhov, V. 1998b. The influence of vegetation-atmosphere-ocean interaction on climate during the mid-Holocene. *Science* **280**, 1916–1919.

Ganopolski, A., Petoukhov, V. K., Rahmstorf, S., Brovkin, V., Claussen, M. and co-authors. 2001. CLIMBER-2: a climate system model of intermediate complexity. Part II: sensitivity experiments. *Clim. Dyn.* **17**, 735–751.

Harvey, L. D. D. 2004. Characterizing the annual-mean climatic effect of anthropogenic CO2 and aerosol emissions in eight coupled atmosphere-ocean GCMs. *Clim. Dynamics* **23**, 569–599.

Haywood, J. M., Stouffer, R. J., Wetherald, R. T., Manabe, S. and Ramaswamy, V. 1997. Transient response of a coupled model to estimated changes in greenhouse gas and sulfate concentrations. *Geophys. Res. Lett.* **24**, 1335–1338.

IPCC, 2001. Climate change 2001: the scientific basis. In: *Contribution of Working Group I to the Third Assessment Report of the Intergovernmental Panel on Climate Change*, (eds J. T. Houghton, Y. Ding, D. J. Griggs, M. Noguer, P. J. van der Linden and co-editors). Cambridge University Press, Cambridge, United Kingdom and New York, NY, USA, 881 pp.

Johns, T. C., Gregory, J. M., Ingram, W. J., Johnson, C. E., Jones, A. and co-authors. 2003. Anthropogenic climate change for 1860 to 2100 simulated with the HadCM3 model under updated emissions scenarios. *Clim. Dyn.* **20**, 583–612.

Jones, A., Roberts, D. L. and Slingo, A. 1994. A climate model study of indirect radiative forcing by anthropogenic sulphate aerosols. *Nature* **370**, 450–453.

Jones, A., Roberts, D. L., Woodage, M. J. and Johnson, C. E. 2001. Indirect sulphate aerosol forcing in a climate model with interactive sulphur cycle. *J. Geophys. Res.* **106**, 20293–20310.

Jones, P. D., Briffa, K. R. and Osborn, T. J. 2003. Changes in the Northern Hemisphere annual cycle: implications for paleoclimatology? *J. Geophys. Res.* **108**, 4588, doi:10.1029/2003JD003695.

Kiehl, J. T. and Briegleb, B. P. 1993. The relative roles of sulfate aerosols and greenhouse gases in climate forcing. *Science* **260**, 311–314.

Kiehl, J. T., Schneider, T. L., Rasch, P. J., Barth, M. C. and Wong, J. 2000. Radiative forcing due to sulfate aerosols from simulations with

the National Center for Atmospheric Research Community Climate Model, Version3. *J. Geophys. Res.* **105**, 1441–1457.

Kinne, S., Schulz, M., Textor, C., Guibert, S., Balkanski, Y. and co-authors 2006. An AeroCom initial assessment - optical properties in aerosol component modules of global models. *Atmos. Chem. Phys.* **6**, 1815–1834.

Lefohn, A. S., Husar, J. D. and Husar, R. B. 1999. Estimating historical anthropogenic global sulfur emission patterns for the period 1850–1990. *Atmos. Environ.* **33**, 3435–3444.

Li, J., Wong, J. G. D., Dobbie, J. S. and Chylek, P. 2001. Parameterization of the optical properties of sulfate aerosols. *J. Atmos. Sciences* **58**, 193–209.

Liou, K. N. 1992. Radiation and cloud processes in the atmosphere: theory, observation, and modeling. *Oxford Monographs on Geology and Geophysics* **20**, Oxford Univ. Press, New York, 487 pp.

Liou, K. N. 2002. An introduction to atmospheric radiation. *International Geophysics Series* **84**, 2nd Edition. Academic Press, Amsterdam, 577 pp.

Lohmann, U. and Lesins, G. 2002. Stronger constraints on the anthropogenic indirect aerosol effect. *Science* **298**, 1012–1015.

Martin, G. M., Johnson, D. W. and Spice, A. 1994. The measurement and parameterization of effective radius of droplets in warm stratocumulus clouds. *J. Atmos. Sci.* **51**, 1823–1842.

Ming, Y., Ramaswamy, V., Ginoux, P. A., Horowitz, L. W. and Russell, L. M. 2005. Geophysical Fluid Dynamics Laboratory general circulation model investigation of the indirect radiative effects of anthropogenic sulfate aerosol. *J. Geophys. Res.* **110**, D22206, doi:10.1029/2005JD006161.

Myhre, G., Highwood E. J., Shine K. P. and Stordal, F. 1998. New estimates of radiative forcing due to well mixed greenhouse gases. *Geophys. Res. Lett.* **25**, 2715–2718.

Myhre, G., Stordal, F., Berglen, T. F., Sundet, J. K. and Isaksen, I. S. A. 2004. Uncertainties in the radiative forcing due to sulfate aerosols. *J. Atmos. Sci.* **61**, 485–498.

Nemesure, S., Wagener, R. and Schwartz, S. E. 1995. Direct shortwave forcing of climate by the anthropogenic sulfate aerosol: sensitivity to particle size, composition, and relative humidity. *J. Geophys. Res.* **100**, 26105–26116.

Peixoto, J. P. and Oort, A. H. 1992. *Physics of Climate*, Springer Verlag, New York, 520 pp.

Petoukhov, V. 1991. *Dynamical–statistical modelling of large-scale climatic processes*. Dr. Sci. thesis, Leningrad Hydrometeorological Institute, St.Petersburg, 431 p. [in Russian].

Petoukhov, V., Ganopolski, A., Brovkin, V., Claussen, M., Eliseev, A. and co-authors. 2000. CLIMBER-2: a climate system model of intermediate complexity. Part I: model description and performance for present climate. *Clim. Dyn.* **16**, 1–17.

Petoukhov, V., Claussen, M., Berger, A., Crucifix, M., Eby, M. and co-authors. 2005. EMIC Intercomparison Project (EMIP-CO2): comparative analysis of EMIC simulations of climate, and of equilibrium and transient responses to atmospheric CO2 doubling. *Clim. Dyn.* **25**, 363–385, doi:10.1007/s00382-005-0042-3.

Pilinis, C., Pandis, S. N. and Seinfeld, J. H. 1995. Sensitivity of direct climate forcing by atmospheric aerosols to aerosol size and composition. *J. Geophys. Res.* **100**, 18739–18754.

Quaas, J., Boucher, O., Dufresne, J.-L. and Le Treut, H. 2004. Impacts of greenhouse gases and aerosol direct and indirect effects on clouds and radiation in atmospheric GCM simulations of the 1930–1989 period. *Clim. Dyn.* **23**, 779–789.

Rahmstorf, S. and Ganopolski, A. 1999. Long-term global warming scenarios computed with an efficient coupled climate model. *Climatic Change* **43**, 353–367.

Randriamiarisoa, H., Chazette, P., Couvert, P., Sanak, J. and Megie, G. 2006. Relative humidity impact on aerosol parameters in a Paris suburban area. *Atmos. Chem. Phys.* **6**, 1389–1407.

Roeckner, E., Bengtsson, L., Feichter, J. Lelieveld, J. and Rodhe, H. 1999. Transient climate change simulations with a coupled Atmosphere-Ocean GCM including the tropospheric sulfur cycle. *J. Climate* **12**, 3004–3032.

Rotstayn, L. D. and Lohmann, U. 2002. Simulation of the tropospheric sulfur cycle in a global model with a physically based cloud scheme. *J. Geophys. Res.* **107**, 4592, doi:10.1029/2002JD002128.

Schneider von Deimling, T., Held, H., Ganopolski, A. and Rahmstorf, S. 2006. Climate sensitivity estimated from ensemble simulations of glacial climate. *Clim. Dyn.* **27**, 149–163, doi:10.1007/s00382-006-0126-8.

Schulz, M., Textor, C., Kinne, S., Balkanski, Y., Bauer, S. and co-authors. 2006. Radiative forcing by aerosols as derived from the AeroCom present-day and pre-industrial simulations. *Atmos. Chem. Phys.* **6**, 5225–5246.

Smith, S. J., Pitcher, H. and Wigley, T. M. L. 2001. Global and regional anthropogenic sulfur dioxide emissions. *Global Planet. Change* **29**, 99–119.

Stier, P., Feichter, J., Kinne, S., Kloster, S., Vignati, E. and co-authors. 2005. The aerosol-climate model ECHAM5-HAM. *Atmos. Chem. Phys.* **5**, 1125–1156.

Takemura, T., Nozawa, T., Emori, S., Nakajima, T. Y. and Nakajima, T. 2005. Simulation of climate response to aerosol direct and indirect effects with aerosol transport-radiation model. *J. Geophys. Res.* **110**, D02202, doi:10.1029/2004JD005029.

Taylor, K. E. and Penner, J. E. 1994. Response of the climate system to atmospheric aerosols and greenhouse gases. *Nature* **369**, 734–737.

Textor, C., Schulz, M., Guibert, S., Kinne, S., Balkanski, Y. and co-authors. 2006. Analysis and quantification of the diversities of aerosol life cycles within AeroCom. *Atmos. Chem. Phys.* **6**, 1777–1813.

Twohy, C. H., Petters, M. D., Snider, R. J., Stevens, B., Tahnk, W. and co-authors. 2005. Evaluation of the aerosol indirect effect in marine stratocumulus clouds: droplet number, size, liquid water path, and radiative impact. *J. Geophys. Res.* **110**, D08203, doi:10.1029/2004JD005116.

Twomey, S. A. 1974. Pollution and the planetary albedo. *Atmos. Environ.* **8**, 1251–1256.